Frontiers in Bioscience Landmark

Front. Biosci. (Landmark Ed) **2026**; 31(7): 52075
https://doi.org/10.31083/FBL52075

Original Research

Lachnospiraceae and Its Metabolite Malate Act in Concert to Repair Gut Microbiota Imbalance and Block Colorectal Cancer Progression

Zejun Fang[1], Yanyan Hu[1], Minjing Zhu[1], Hengming Mei[1], Chaoju Gong[2], Jiaoe Chen[3,*]

[1]Central Laboratory, Sanmen People's Hospital, Sanmenwan Branch, The First Affiliated Hospital, Zhejiang University School of Medicine, 317100 Taizhou, Zhejiang, China
[2]Central Laboratory, The Affiliated Xuzhou Municipal Hospital of Xuzhou Medical University, 221002 Xuzhou, Jiangsu, China
[3]Department of Gastroenterology, Sanmen People's Hospital, 317100 Taizhou, Zhejiang, China
*Correspondence: chenjiaoe@zjsmyy.com (Jiaoe Chen)
Academic Editor: Jordi Sastre-Serra
Submitted: 20 March 2026 Revised: 29 May 2026 Accepted: 16 June 2026 Published: 27 July 2026

Abstract

Background: Gut microbiota dysbiosis is a crucial driver of the initiation and progression of colorectal cancer (CRC), where functional gut microbes and their metabolites play key roles in the microecological regulation of CRC. Currently, the association between *Lachnospiraceae* and CRC progression, as well as the underlying mechanisms, remains incompletely understood and warrants further investigation. **Methods:** Bioinformatics analysis was performed to explore the co-pathway association between gut microbiota and metabolites in CRC patient samples. *In vivo* animal models were established to assess the regulatory effects of *Lachnospiraceae* on CRC tumorigenesis and gut microbiota homeostasis. The anti-CRC activities of *Lachnospiraceae* and its metabolite malate were investigated using *in vitro* experiments that measured cell viability, proliferation, apoptosis, and colony formation. Western blotting was performed to detect the expression levels of key proteins in the Wingless/Integrated (Wnt)/β-catenin signaling pathway. **Results:** Bioinformatics analysis revealed that malate was significantly downregulated in CRC patients, accompanied by gut microbiota dysbiosis driven predominantly by short-chain fatty acid (SCFA)-related Firmicutes such as *Lachnospiraceae* and *Ruminococcaceae*. *In vivo*, *Lachnospiraceae* restored gut microbiota homeostasis, reduced tumor number, and decreased tumor load. *In vitro*, *Lachnospiraceae* suppressed colorectal tumorigenesis and increased colonic D-malate levels. **Conclusion:** *Lachnospiraceae* bacterium biologics abstracts accession-2278 (BAA-2278) is associated with anti-CRC effects in preclinical models, potentially mediated through regulation of gut microbiota homeostasis and inhibition of Wnt/β-catenin signaling via its metabolite malate.

Keywords: colorectal neoplasms; *Lachnospiraceae*; malate; gastrointestinal microbiota; beta-catenin

1. Introduction

Colorectal cancer (CRC), one of the malignant tumors with persistently high incidence and mortality worldwide and the second leading cause of cancer-related death, imposes a heavy burden on the global healthcare system [1,2]. The intricate pathogenesis of CRC involves a critical interplay between environmental factors and host intrinsic factors. Gut microbiota dysbiosis, a core component of the human microecological system, has been identified as a key driver of CRC initiation and progression [3,4]. Accumulating studies have demonstrated that gut microbiota contribute to CRC pathophysiology through multiple pathways such as metabolite regulation and immune microenvironment remodeling, thereby providing novel microecological targets for the prevention and treatment of CRC [5,6,7].

Functional microbiota and their metabolites are central to intestinal microecological regulation. *Lachnospiraceae*, a common beneficial bacterial family in the intestine, has been confirmed to be closely associated with reduced risk of CRC [8]. Existing research has found that tumor-resident *Lachnospiraceae* can inhibit colorectal carcinogenesis by enhancing tumor immune surveillance and regulating the body's immune response [9,10]; however, their specific functional targets and downstream regulatory mechanisms remain incompletely elucidated. Bioinformatics analyses in this study revealed the presence of multiple metabolite disorders in CRC patients, with malate identified as a key differential metabolite. Recent studies have confirmed that malate induces cell cycle arrest in CRC cells [11]. In addition, malate not only modulates the homeostasis of gut microbiota but also maintains the functional activity of cytotoxic T cells in the tumor microenvironment [12,13], suggesting its potential involvement in the pathological regulation of CRC. However, the specific role and origin of malate in CRC have not yet been clarified.

To address this knowledge gap, this study first analyzed the associations between microbiota and metabolites in CRC patient samples via bioinformatic analysis, with a focus on confirming malate downregulation and identifying its potential microbial drivers. Subsequently, *in vitro* and *in vivo* experiments were conducted to verify the regulatory effects of *Lachnospiraceae* and malate on CRC tumorige-

nesis. This study aimed to elucidate the anti-CRC mechanism of the *Lachnospiraceae*-malate-gut microbiota regulatory axis, thereby providing novel theoretical evidence and candidate targets for microecological intervention in CRC.

2. Materials and Methods

2.1 Data Sources for Bioinformatics Analysis

16S rRNA sequencing data were sourced from the public research data of Ternes et al. [14], including samples from the healthy control (HC) group and CRC group, which were used for the analysis of gut microbiota structure and function.

Metabolomics data were sourced from the public research data of Gao et al. [15]. Fasting serum samples were collected from 34 HC and 35 CRC patients, and metabolomics detection data were acquired via liquid chromatography-tandem mass spectrometry (LC-MS/MS) technology.

2.2 16S rRNA Sequencing Data Analysis

2.2.1 Analysis Software and Databases

A set of specialized bioinformatics tools was employed for a comprehensive analysis of 16S rRNA sequencing data, including QIIME2 2023.2 (Caporaso Lab, Northern Arizona University, Flagstaff, AZ, USA), DADA2 1.26 (Callahan BJ, North Carolina State University, Raleigh, NC, USA), PICRUSt2 2.5.1 (Langille MGI, Dalhousie University, Halifax, NS, Canada), MicrobiotaProcess 1.18 (R package, Bioconductor, Fred Hutchinson Cancer Research Center, Seattle, WA, USA), treeio 1.30 (R package, Bioconductor, Fred Hutchinson Cancer Research Center, Seattle, WA, USA), and microeco 1.15 (R package, GitHub, University of Chinese Academy of Sciences, Beijing, China). Taxonomic annotation of 16S rRNA gene sequences was performed using the SILVA V138 database (https://www.arb-silva.de/, Leibniz Institute DSMZ, Braunschweig, Germany).

2.2.2 Data Preprocessing

Sequencing quality assessment was performed to ensure downstream reliability. The depth and quality of forward and reverse reads were visually analyzed to identify potential biases or artifacts.

Based on quality results, DADA2 was used to truncate high-quality fragments to 260 bp (forward) and 220 bp (reverse). Non-target taxa (e.g., chloroplasts, mitochondria), low-abundance features (<10 counts), and occasional features present in <5 samples were further filtered out.

DADA2 was then applied for sequence quality control, denoising, paired-end merging, and chimera removal to infer single-nucleotide resolution Amplicon Sequence Variants (ASVs). Taxonomic annotation (domain to species level, where uniquely matched) was performed using a Naive Bayes classifier trained on the SILVA 16S V3-V4 (341F/806R) region from the SILVA V138 database (https://www.arb-silva.de/), hosted by the Leibniz Institute DSMZ.

2.2.3 Microbial Diversity Analysis

Alpha diversity analysis, reflecting within-sample microbial diversity, involved calculation of multiple indices including Observe, Chao1, Abundance-based Coverage Estimator (ACE), Shannon, Simpson, and Pielou to assess species richness and evenness. Rarefaction curves were generated to verify the rationality of the sequencing data volume, ensuring that there was sufficient depth to capture the majority of microbial taxa present in the samples.

Beta diversity analysis was performed to evaluate differences in microbial community structure between groups. Bray-Curtis distances were calculated to quantify dissimilarities among samples, and Adonis analysis was used to test the statistical significance of group-level differences. Principal Coordinate Analysis (PCOA) was employed for visualization, clearly distinguishing microbial community structure between the HC and CRC groups.

2.2.4 Species Composition and Differential Analysis

Species composition analysis was performed at both the genus and species levels to characterize the gut microbiota in the HC and CRC groups. Visualization methods including distribution plots and relative abundance heatmaps were used to identify dominant microbial taxa and illustrate differences in community composition between groups, providing an overview of microbial distribution patterns.

Differential microbial screening was conducted using the microeco package in R with the Linear Discriminant Analysis Effect Size (LEfSe) method. Then, the taxonomic differences were analyzed at both the genus and species levels between the HC and CRC groups, enabling the identification of significantly different taxa that served as potential biomarkers for distinguishing the two groups.

2.2.5 Prediction of Microbial Functional Pathways

PICRUSt2 software was used to predict microbial functional pathways based on the ASV relative abundance table and representative sequences, combined with microbial genome databases. The ggpicrust2 1.7.2 (R package, GitHub, Dalhousie University, Halifax, NS, Canada) was employed to perform differential analysis using the LinDA method, enabling the screening of significantly differential functional pathways between the HC and CRC groups.

2.3 Untargeted Metabolomics Data Analysis

2.3.1 Data Preprocessing and Differential Metabolite Screening

Multivariate statistical analysis was performed using the ropls 1.32 (R package, Bioconductor, CEA, Paris, France) to evaluate the overall separation trend of metabolites between the HC and CRC groups. Principal Component Analysis (PCA) was used for unsupervised pat-

tern recognition, while Orthogonal Partial Least Squares-Discriminant Analysis (OPLS-DA) was applied as a supervised model to enhance the discrimination between the two groups.

Prior to differential analysis, the metabolite abundance matrix was transformed using $\log_2(X+1)$ to normalize the data distribution. The limma 3.54 (R package, Bioconductor, Walter and Eliza Hall Institute, Melbourne, VIC, Australia) was then utilized to identify differentially abundant metabolites between the HC and CRC groups. Metabolites were considered significantly differential, with significance thresholds set at $|\log_2$ fold change (FC)$| > 0$, p-value < 0.05, and Variable Importance in Projection (VIP) value >1, ensuring the reliability and biological relevance of the selected metabolites.

2.3.2 Functional Pathway Enrichment Analysis

The Kyoto Encyclopedia of Genes and Genomes (KEGG) REST package and MetaCyc database (https://metacyc.org/, SRI International, Menlo Park, CA, USA) were separately used for functional pathway enrichment analysis of upregulated and downregulated differential metabolites. This analysis aimed to reveal the core biological processes and metabolic pathways involving these differential metabolites.

2.4 Correlation Analysis Between Differential Microbiota and Differential Metabolites

2.4.1 Co-Pathway Analysis

Since 16S rRNA sequencing data and metabolomics data were derived from different studies, co-pathway analysis was used as an alternative to direct correlation analysis. Functional pathways predicted from 16S rRNA data and MetaCyc pathways enriched from metabolomics data were separately classified into upregulated and downregulated groups. Significantly enriched pathways were filtered using the Benjamini-Hochberg (BH) correction with a false discovery rate (FDR) <0.05. The intersections of upregulated and downregulated pathways between the two datasets were calculated to identify common pathways.

2.4.2 Identification of Core Contributors to Common Pathways

Based on the stratified pathway contribution table from Phylogenetic Investigation of Communities by Reconstruction of Unobserved States 2 (PICRUSt2), the contribution of different microbial taxa to common pathways was quantified. For each taxon in each group, three indicators were calculated: mean absolute contribution, mean relative contribution, and prevalence. The Wilcoxon rank-sum test combined with BH correction was used to screen core microbial taxa that significantly contributed to common pathway differences. The screening criteria were as follows: for CRC-upregulated pathways, the prevalence in CRC group (prev_CRC) ≥0.30 (a widely accepted threshold in core microbiota identification to ensure taxon ubiquity while avoiding overly stringent exclusion of functionally relevant low-abundance taxa [16,17]), and the mean relative contribution in CRC group (mean_rel_CRC) ≥0.02 (corresponding to ≥2% relative abundance, a conservative cutoff established in previous PICRUSt2-based functional contribution analyses to filter out taxa with marginal metabolic impact [18]); for CRC-downregulated pathways, the prevalence in HC group (prev_HC) ≥0.30, and the mean relative contribution in HC group (mean_rel_HC) ≥0.02.

2.4.3 Validation of Common Pathway Metabolites

For the significantly identified common pathways, the enriched metabolites were extracted. Box plots were employed to visualize the differences in expression levels of these metabolites between the HC group and CRC group, verifying the association between metabolites and pathways as well as the intergroup expression characteristics.

2.5 Animal Ethics

The animal experiments conducted in this study strictly adhered to the Guidelines for Ethical Review of Laboratory Animal Welfare and were approved by the Laboratory Animal Ethics Review Committee of Laboratory Animal Welfare and were approved by the Laboratory Animal Ethics Review Committee of Zhejiang Provincial Laboratory Animal Center (ZJCLA-IACUC-20011391). Male C57BL/6 mice (5 weeks old, 18–22 g, n = 16) were purchased from Hangzhou Medical College, China. All mice were housed in a specific pathogen-free (SPF) animal facility with controlled conditions: 22 ± 2 ℃, relative humidity of 54 ± 5%, and a 12-hour light-dark cycle. Mice had free access to standard laboratory chow and sterile drinking water throughout the experiment. The study was designed and performed in accordance with the "3R" principle (Replacement, Reduction, Refinement) to minimize animal suffering and ensure scientific rigor. Sample size of 8 mice per group was determined based on established standards for AOM/DSS CRC models in gut microbiota intervention studies [19], which have been demonstrated to yield sufficient statistical power for detecting biologically meaningful differences in tumor burden and molecular markers.

2.6 Establishment of CRC Mouse Model and Grouping

Lachnospiraceae bacterium (Lb; BAA-2278, ATCC, USA) was used in this study and cultured under anaerobic conditions at 37 ℃ (ZDYY-III, Shanghai Chuanyu Experimental Instrument Co., Ltd., Shanghai, China). Bacteria were harvested by centrifugation at 6000 ×g for 10 minutes, then resuspended in brain heart infusion (BHI; HY-157355, MCE, Monmouth Junction, NJ, USA) broth to a final concentration of 1×10^8 colony-forming units (CFU)/100 µL for subsequent gavage [20]. BHI broth alone served as a blank control, and its preparation followed standard laboratory protocols.

A carcinogen-induced CRC mouse model was established as previously described with minor modifications [20]. Male C57BL/6 mice were intraperitoneally injected with a single dose of azoxymethane (AOM; HY-111375, MCE, Monmouth Junction, NJ, USA) at 10 mg/kg body weight. One week after AOM injection, mice were given drinking water containing 1% dextran sodium sulfate (DSS; A600160, Sangon Biotech, Shanghai, China) for 7 consecutive days to induce intestinal mucosal injury and promote tumorigenesis.

Seven days after DSS withdrawal, mice were randomly divided into two groups (n = 8 per group) using a random number table by an independent investigator not involved in subsequent data collection or analysis: BHI Group (daily gavage with 100 µL of sterile BHI broth); and Lb Group (daily gavage with 100 µL of *Lachnospiraceae* suspension (1×10^8 CFU)) [20,21]. The gavage treatment was continued for 17 weeks. During the experimental period, the general condition, body weight, and food/water intake of mice were monitored regularly. For histological assessment (hematoxylin and eosin [HE] staining, Terminal Deoxynucleotidyl Transferase mediated dUTP Nick-End Labeling [TUNEL], and MKi-67 [Ki-67] immunohistochemistry), D-malate concentration measurement, and data analysis, investigators were blinded to group allocation. Tissue samples were coded by an independent researcher prior to processing, and codes were revealed only after completion of all data collection and statistical analyses.

After 17 weeks of treatment, mice were anesthetized with 5% isoflurane (HY-A0134, MCE, Monmouth Junction, NJ, USA, v/v) in medical oxygen (flow rate: 1.0 L/min) via a dedicated animal anesthesia induction chamber for 3–5 min until the loss of the righting reflex and pedal withdrawal reflex was observed (confirming a deep plane of anesthesia). After the completion of relevant operations, mice were euthanized by cervical dislocation under deep 5% isoflurane anesthesia to minimize animal suffering. The entire colon was rapidly isolated to record its length and gross morphology, and tumor number and size were measured for tumor load calculation. Single tumor volume = $(4/3) \times \pi \times (r)^3$, where r is the radius of the tumor [20]. The final total tumor load = the sum of the volumes of all tumors in the colon of each mouse. Colon tissues from proximal, middle, and distal segments were processed as follows: one portion was fixed in 4% paraformaldehyde (P0099, Beyotime, Shanghai, China) for HE staining, TUNEL, and Ki67 immunohistochemical analyses; another portion was stored at –80 ℃ for D-malate concentration detection.

2.7 Cell Culture Experiments

Human CRC HCT116 cells (AW-CELLS-H0110) were purchased from the Shanghai Anwei Biotechnology Co., Ltd. (China) and cultured in McCOY's5A medium (PM150710, Procell, Wuhan, Hubei, China) supplemented with 10% fetal bovine serum (FBS; 10100139, ThermoFisher Scientific, Waltham, MA, USA) and 1% penicillin-streptomycin (C0222, Beyotime, Shanghai, China). All cell lines were validated by STR profiling and tested negative for mycoplasma.

Lachnospiraceae was anaerobically cultured in BHI broth at 37 ℃, and centrifuged (6000 ×g, 10 min). The supernatant was filtered through a 0.22 µm membrane (GTTP14250, Millipore, Billerica, MA, USA). The filtrate was diluted to 10% (v/v) with McCOY's5A to prepare *Lachnospiraceae* bacterium-derived conditioned medium (Lb-CM). D-(+)-Malic acid (02300, Sigma-Aldrich, St. Louis, MO, USA) was dissolved in sterile phosphate buffer saline (PBS; ST477, Beyotime, Shanghai, China) to a 150 mM stock solution (filtered sterilized), then diluted to a working concentration of 15 mM with McCOY's5A [22]. BHI broth underwent the same centrifugation/filtration as Lb-CM and was diluted to 10% (v/v) as the BHI control solution.

HCT116 cells were seeded into appropriate culture plates (5×10^3 cells/well) and allowed to adhere for 24 h. Cells were then randomly divided into four groups: Control (10 % sterile PBS in McCOY's5A), BHI (10% BHI control solution in McCOY's5A), Lb-CM (10% Lb-CM in McCOY's5A), and D-malate (15 mM D-(+)-Malic acid in McCOY's5A). All groups were cultured under the same conditions (37 ℃, 5% CO_2) for 24 h.

2.8 Biochemical Enzymatic Colorimetric Assay

Lachnospiraceae bacterium (BAA-2278, ATCC, Manassas, VA, USA) was anaerobically cultured in BHI broth at 37 ℃ for the same duration as the cell culture experiments. Sterile BHI broth without bacterial inoculation was incubated under identical conditions as a negative control. After cultivation, bacterial cultures and sterile BHI controls were centrifuged at 6000 ×g for 10 minutes, and the supernatants were collected and filtered through a 0.22 µm membrane (GTTP14250, Millipore, Billerica, MA, USA). The D-malate concentration in the filtered supernatants was determined using the D-malate test kit (K-DMAL, Megazyme, Ireland) according to the manufacturer's instructions. Briefly, the reaction mixture containing D-malate dehydrogenase and nicotinamide adenine dinucleotide (NAD^+) was added to the supernatant samples, and the absorbance at 340 nm was measured using a microplate reader (Varioskan LUX, Thermo Fisher Scientific, Waltham, MA, USA) to quantify NADH formation, which is stoichiometrically proportional to D-malate concentration. D-malate levels were calculated based on a standard curve generated using D-malate standards (0–50 µM) run in parallel with the samples. All measurements were performed in triplicate.

2.9 HE Staining

Colon tissue samples from each group were fixed in 4% paraformaldehyde for 24 h, followed by conven-

tional dehydration, paraffin embedding, and serial sectioning (5 μm thickness). After rehydration, sections were stained with hematoxylin (C0107, Beyotime, Shanghai, China) for 5 min, rinsed with tap water, and counterstained with eosin (C0109, Beyotime, Shanghai, China) for 2 min. Following dehydration and transparentization, the sections were sealed with neutral gum (C0173, Beyotime, Shanghai, China). Pathological changes were observed under an optical microscope (200×, Nikon Ts2R-FL, Nikon Corporation, Tokyo, Japan) to assess colorectal tissue hyperplasia.

2.10 Terminal Deoxynucleotidyl Transferase mediated dUTP Nick-End Labeling (TUNEL)

After deparaffinization and gradient rehydration, paraffin-embedded sections of colon tissue were stained as per the instructions of the TUNEL Apoptosis Detection Kit (C1091, Beyotime, Shanghai, China). TdT enzyme reaction solution was added for incubation at 37 ℃ for 60 minutes. After the reaction was terminated, nuclei were stained with hematoxylin for 5 minutes, and sections were dehydrated and transparentized. Images were observed and captured under a microscope. Three random high-power fields (200×) were selected, and the number of apoptotic cells and total cells was counted using ImageJ (version 1.52v, National Institutes of Health, Bethesda, MD, USA) software to calculate the apoptosis level.

2.11 Immunohistochemistry

Colon paraffin sections (5 μm) were deparaffinized, rehydrated, and antigen-retrieved. Endogenous peroxidase was blocked with 3% hydrogen peroxide (88597, Millipore, Burlington, MA, USA) for 10 min at room temperature, followed by 60-min blockage with 5% Bovine Serum Albumin (BSA; HY-D0842, MCE, Monmouth Junction, NJ, USA). Sections were incubated overnight at 4 °C with Ki67 primary antibody (1:200, ab16667, Abcam, Cambridge, UK), and then with HRP-conjugated secondary antibody (1:500, ab6721, Abcam, Cambridge, UK) for 30 min at room temperature. Signals were visualized with 3,3′-diaminobenzidine (DAB) substrate (HY-W014212, MCE, Monmouth Junction, NJ, USA). Sections were counterstained with hematoxylin, dehydrated, transparentized, and mounted. Images (200×) were captured, with Ki67-positive/total cells quantified via ImageJ to calculate the positive area.

2.12 D-Malate Concentration

D-malate concentration in colon tissues was measured using the D-malate test kit (K-DMAL, Megazyme, Bray, Wicklow, Ireland), following procedures described in previous literature [23]. Briefly, colon tissue samples were homogenized and centrifuged to collect supernatants. The kit's reaction mixture was added to supernatants, and absorbance was measured at 340 nm using a microplate reader (Varioskan LUX, Thermo Fisher Scientific, Waltham, MA, USA). D-malate levels were calculated based on the standard curve generated alongside samples.

2.13 Cell Counting Kit-8 (CCK-8)

For the CCK-8 cell viability assay, treated HCT116 cells were plated into 96-well culture plates (FCP962, Beyotime, Shanghai, China) at a density of 5×10^3 cells per well. Following 24 hours of incubation under standard conditions, 10 μL of CCK-8 reagent (HY-K0301, MCE, Monmouth Junction, NJ, USA) was added to each well, and the plates were further incubated at 37 °C for another 2 hours. Finally, a microplate reader was used to measure the absorbance at 450 nm, which was used to evaluate relative cell viability.

2.14 5-Ethynyl-2′-deoxyuridine (EdU)

For the EdU cell proliferation assay (C0081L, Beyotime, Shanghai, China), treated HCT116 cells (2×10^5 cells/well in 6-well plates (FCP606, Beyotime, Shanghai, China)) were cultured overnight, and processed as per the kit's protocol. Proliferating cells were labeled with Azide 647 (red fluorescence), and nuclei were counterstained with 4′,6-Diamidino-2′-phenylindole (DAPI; C1005, Beyotime, Shanghai, China; blue fluorescence). Images (200×) were captured under an inverted fluorescence microscope (Leica, DM IL, Leica Microsystems, Wetzlar, Germany), and the number of EdU-positive cells was counted from three randomly selected high-power fields per group.

2.15 Flow Cytometry

Harvested cells were gently washed twice with precooled PBS, resuspended in 600 μL flow cytometry binding buffer (C1711, Beyotime, Shanghai, China) at 1×10^6 cells/mL, sequentially stained with 5 μL Annexin V-fluorescein isothiocyanate (FITC) and 5 μL propidium iodide (PI) (C1062S, Beyotime, Shanghai, China), incubated at room temperature in the dark for 15 min, and analyzed for apoptosis using a FACSCalibur flow cytometer (BD Biosciences, Franklin Lakes, NJ, USA). Cells were gated on forward scatter (FSC) versus side scatter (SSC) to exclude debris, and apoptotic cells were identified as Annexin V^+/PI^- (early apoptosis) or Annexin V^+/PI^+ (late apoptosis). Data were analyzed using FlowJo software.

2.16 Colony Formation Experiment

After precipitation, cells were counted, diluted to 1×10^3 cells/mL, and seeded into 6-well plates at 200 cells/well for incubation. Post-adhesion, cells received the designated treatments and were cultured for 2–3 weeks. Upon visible colony formation, the culture was terminated. Wells were gently washed 2–3 times with PBS, fixed with 1 mL methanol (C06901102, Nanjing Reagent, Nanjing, Jiangsu, China) for 15 min, stained with 1 mL Giemsa dye (C0133, Beyotime, Shanghai, China) for 30 min, and rinsed with running water. Colonies were counted microscopically, and the percentage of colony number was counted.

2.17 Plasmid Transfection

The full-length human *β-catenin* coding sequence (NM_001098210) was cloned into the pcDNA3.1(+) expression vector (Invitrogen, Waltham, MA, USA) to generate the *β-catenin* overexpression plasmid (pcDNA3.1-*β-catenin*). The empty pcDNA3.1(+) vector served as a negative control (NC). HCT116 cells were seeded into 6-well plates (FCP606, Beyotime, Shanghai, China) at a density of 2×10^5 cells/well and cultured overnight to reach 70–80% confluence. Cells were then randomly divided into three groups: Control (untreated), NC (transfected with empty pcDNA3.1 vector), and *β-catenin* (transfected with pcDNA3.1-*β-catenin*). Transfection was performed using Lipofectamine 3000 transfection reagent (L3000015, Thermo Fisher Scientific, Waltham, MA, USA) according to the manufacturer's protocol. Briefly, 2.5 μg of plasmid DNA and 5 μL of P3000 reagent were diluted in 125 μL of Opti-MEM reduced serum medium (31985062, Gibco, Waltham, MA, USA), and 3.75 μL of Lipofectamine 3000 was diluted in another 125 μL of Opti-MEM. The two mixtures were combined, incubated at room temperature for 15 minutes, and then added dropwise to the cells. After 6 hours, the transfection medium was replaced with fresh McCoy's 5A complete medium, and cells were cultured for an additional 48 hours.

2.18 Western Blot

Cells were lysed with radioimmunoprecipitation buffer (PC901, Biomiga, San Diego, CA, USA) for protein extraction, and protein concentration was quantified using a bicinchoninic acid assay kit (KGP903, KeyGEN, Nanjing, Jiangsu, China). Proteins were separated using sodium dodecyl sulfate-polyacrylamide gel electrophoresis (P0012A, Beyotime, Shanghai, China), transferred to polyvinylidene fluoride membranes (2215, Millipore, Burlington, MA, USA), and blocked with 5% skimmed milk at 37 °C for 2 h. Membranes were incubated overnight at 4 °C with primary antibodies against β-catenin (1:1000, ab32572, Abcam, Cambridge, UK), Myelocytomatosis oncogene (c-Myc; 1:1000, #5605, Cell Signaling Technology, Danvers, MA, USA), and matrix metallopeptidase 7 (MMP7; 1:1000, ab207299, Abcam, Cambridge, UK), and β-actin (as internal control; 1:2000, ab8226, Abcam, Cambridge, UK), followed by culture with secondary antibodies (1:5000, ab205719, Abcam, Cambridge, UK) at room temperature. Bands were visualized using ECL reagent (P0018FS, Beyotime, Shanghai, China) and an iBright CL750 imaging system (Thermo Fisher Scientific, Waltham, MA, USA).

2.19 Statistical Analysis

Statistical analyses were performed using GraphPad Prism 8.0 (GraphPad Software, San Diego, CA, USA) software. Quantitative data are expressed as mean ± standard deviation (SD). The number of biological replicates is indicated in each figure legend (n = 3 for *in vitro* experiments; n = 8 for *in vivo* experiments). Comparisons between two groups were conducted with an independent samples *t*-test, while multi-group comparisons were performed with one-way analysis of variance (ANOVA) followed by Tukey's post-hoc test. A p value < 0.05 was considered statistically significant.

3. Results

3.1 Gut Microbiota Diversity Alterations in CRC Patients

This study first analyzed the differences in intestinal microbiota diversity and community structure between the HC group and CRC group using 16S rRNA sequencing data. In the α-diversity analysis, rarefaction curves plateaued for all samples, indicating sufficient sequencing depth to cover most microbial species in the samples and supporting their suitability for subsequent analyses (Fig. 1A,B). Quantitative results of α-diversity indices showed that the Observed species, Chao1, ACE, Shannon, Simpson, and Pielou indices in the CRC group were significantly lower than those in the HC group (Fig. 1C, $p < 0.05$). Decreases in the Observed species richness, Chao1 index, and ACE index suggested reduced species richness of gut microbiota in CRC patients, while reductions in the Shannon, Simpson, and Pielou indices indicated decreased community evenness in the CRC group, collectively reflecting significant impairment of gut microbiota diversity in CRC patients (Fig. 1C, $p < 0.05$). For β-diversity analysis, Bray-Curtis distances combined with PCOA were used for visualization (Fig. 1D). The results showed that the first principal coordinate (PCo1) explained 8.63% of the variation in community structure, and samples from the HC and CRC groups exhibited a clear clustering separation trend in the PCOA plot, indicating inherent differences in gut microbiota community structure between the two groups (Fig. 1D). Together, these findings confirmed that the development of CRC was closely associated with reduced gut microbiota diversity and disrupted community structure.

3.2 Analysis of Gut Microbiota Composition at Genus and Species Levels

To systematically analyze the differences in gut microbiota composition between the HC group and CRC group, this study investigated species distribution and relative abundance at both the genus and species levels. Substantial individual differences were observed in microbiota composition among samples from the two groups; however, common dominant genera (e.g., *Bacteroides*) accounted for a high proportion in most samples, while a small number of samples exhibited a "subtype" distribution dominated by other genera (Fig. 2A,E). Group-averaged analysis revealed that compared with the HC group, the CRC group showed a higher relative abundance of potential opportunistic pathogens such as *Escherichia-Shigella* (Fig. 2B,F). The heatmap of genus-level relative abundance further illustrated the distribution patterns of high-abundance gen-

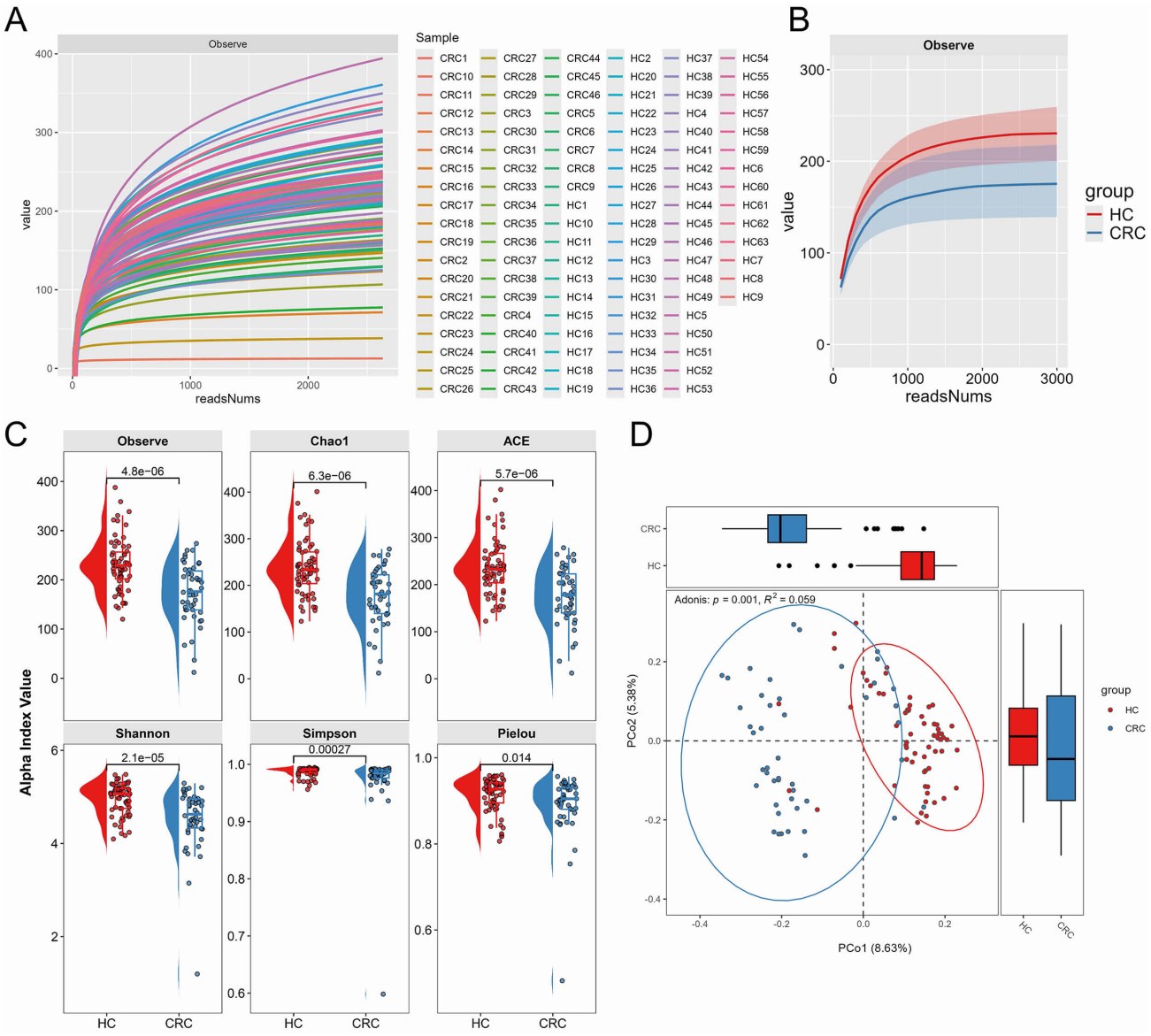

Fig. 1. Intestinal microbial diversity analysis of healthy control (HC) and colorectal cancer (CRC) groups. (A) Individual sample rarefaction curves (x-axis: sequencing reads; y-axis: observed Amplicon Sequence Variants (ASVs)). Curve plateau indicates sufficient sequencing depth. (B) Grouped rarefaction curves (HC: red; CRC: blue; x-axis: sequencing reads; y-axis: mean observed ASVs). (C) Alpha diversity index comparison (Observed species, Chao1, Abundance-based Coverage Estimator (ACE), Shannon, Simpson, Pielou). Each dot represents a sample; horizontal lines indicate medians. (D) Principal Coordinate Analysis (PCOA) of beta diversity based on Bray-Curtis distances (x-axis: PCo1, 8.63% variation; y-axis: PCo2). HC (red) and CRC (blue) samples form a distinct cluster (significant intergroup difference by Adonis). Sample sizes: n = 63 (HC group), n = 46 (CRC group). Analyses were performed using R packages MicrobiotaProcess 1.18 (alpha diversity) and microeco 1.15 (beta diversity).

era across different samples, and the grouped heatmap presented the clustering differences in the abundance of dominant genera between the two groups (Fig. 2C,D). Red and blue gradients clearly distinguished high- versus low-abundance microbiota between groups (Fig. 2C,D). At the species level, the relative abundance heatmap and grouped heatmap results showed that multiple potential pathogenic species were specifically enriched in the CRC group (e.g., *Pseudomonas guguanensis* was more abundant in the CRC group), and samples from the two groups exhibited obvious clustering separation in the grouped heatmap (Fig. 2G,H).

3.3 Characteristics of Differential Taxa and Functional Pathways in Intestinal Microbiota

Through differential analysis and functional prediction, this study probed into the differences in microbial taxa and functional pathways of intestinal microbiota between the HC and CRC groups. The LEfSe method was used to screen differential microbiota at both the genus and

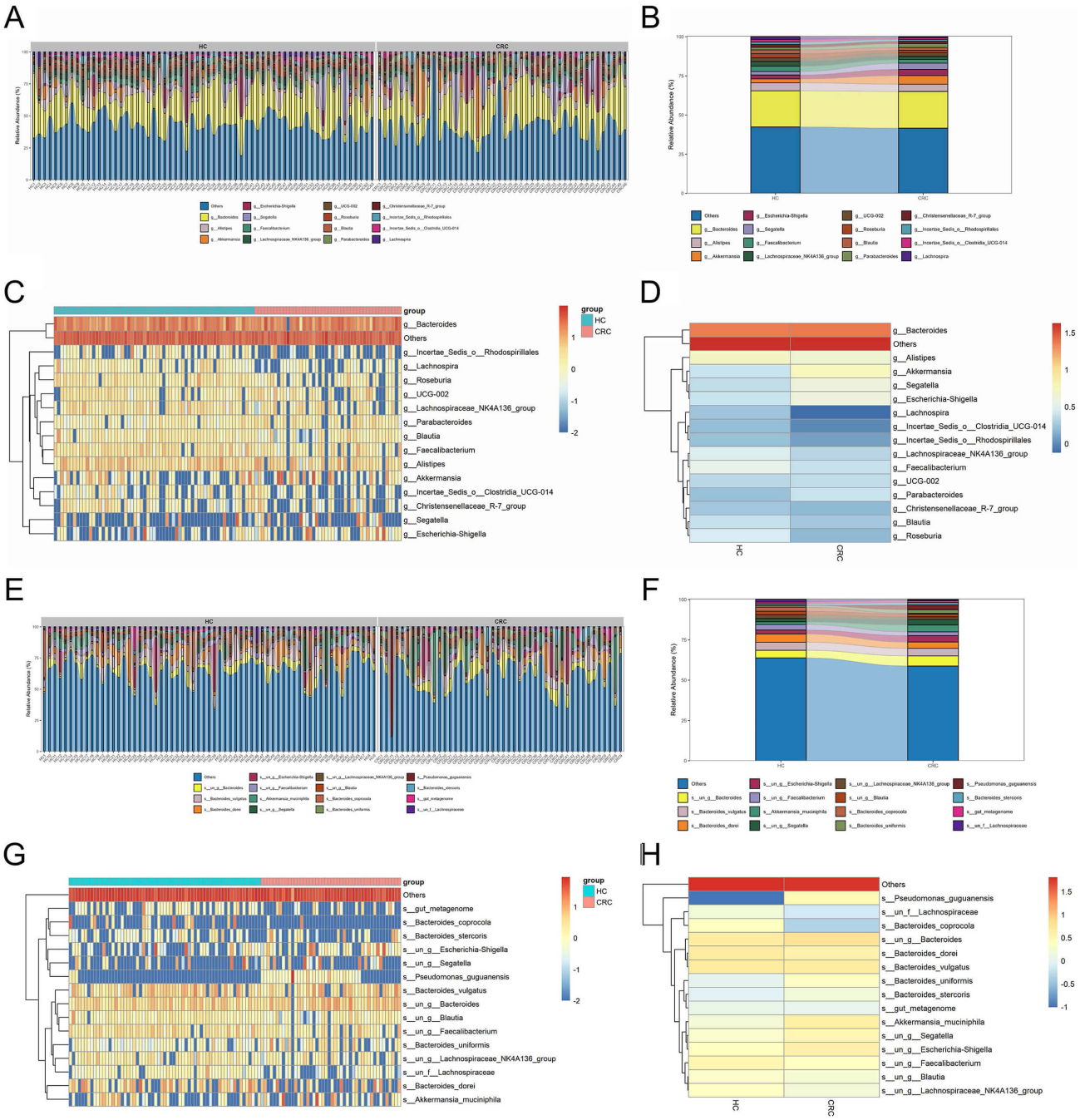

Fig. 2. Composition and abundance characteristics of intestinal microbiota at the genus and species levels between HC and CRC groups. (A) Genus-level distribution of individual samples (color-coded by genus). (B) Grouped genus-level average distribution (HC vs. CRC; color-coded by genus). (C) Genus-level relative abundance heatmap (rows: top genera; columns: individual samples). (D) Grouped genus-level relative abundance heatmap (samples clustered by group; color gradient indicates relative abundance). (E) Species-level distribution of individual samples (color-coded by species). (F) Grouped species-level average distribution (HC vs. CRC; color-coded by species). (G) Species-level relative abundance heatmap (rows: top species; columns: individual samples). (H) Grouped species-level relative abundance heatmap (samples clustered by group; color gradient indicates relative abundance). Sample sizes: n = 63 (HC group), n = 46 (CRC group).

species levels (Fig. 3A,B). At the genus level, potential pathogenic genera such as *Pseudomonas* and *Escherichia-Shigella* in the CRC group had significantly higher Linear Discriminant Analysis (LDA) scores than those in the HC group, while the HC group was enriched with beneficial genera (e.g., *Lachnospiraceae*_NK4A136_group, *Faecalibacterium*) that produced short-chain fatty acids (Fig. 3A). A consistent pattern was observed at the species

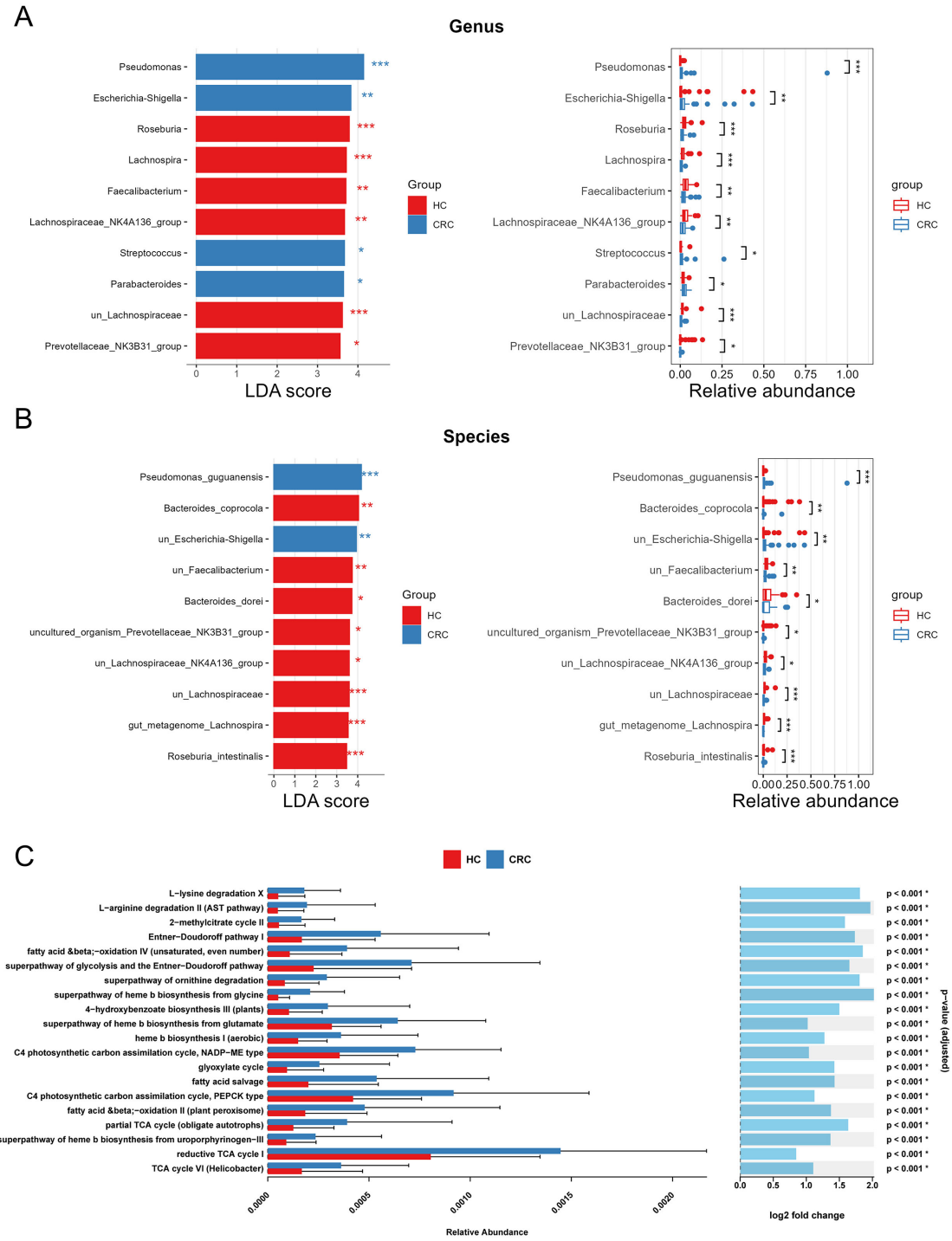

Fig. 3. Differential microbial taxa and functional pathways between HC and CRC groups. (A) Genus-level Linear discriminant analysis Effect Size (LEfSe) analysis. Left: Linear Discriminant Analysis (LDA) score plot (threshold >3; red = HC-enriched, blue = CRC-enriched); Right: Relative abundance plot (dots represent individual samples; boxplots show group distribution). (B) Species-level LEfSe analysis. Left: LDA score plot (threshold >3; red = HC-enriched, blue = CRC-enriched); Right: Relative abundance plot (dots represent individual samples; boxplots show group distribution). (C) Differential functional pathways (TOP20) predicted by PICRUSt2. Left: Relative abundance of pathways (red = HC, blue = CRC); Right: $\log_2$ fold change (false discovery rate (FDR) <0.001) of CRC vs. HC, showing upregulated pathways in CRC. Sample sizes: n = 63 (HC group), n = 46 (CRC group), $^{*}p < 0.05$, $^{**}p < 0.01$, $^{***}p < 0.001$ vs. the HC group.

level: pathogenic species like *Pseudomonas guguanensis* were more abundant in the CRC group, whereas beneficial species such as *Bacteroides dorei* were enriched in the HC group (Fig. 3B). The relative abundance plots visually showed the intergroup abundance differences of these taxa, indicating that the intestinal microbiota of the CRC group was characterized by "pathogen enrichment and beneficial bacteria depletion" (Fig. 3A,B).

For functional pathway differences, functions of microbiota were predicted via PICRUSt2 and analyzed for differential expression using LinDA. Results showed that the top 20 upregulated pathways in the CRC group were mainly associated with core metabolic processes: energy and carbon metabolism (e.g., reductive TCA cycle I, glyoxylate cycle), fatty acid metabolism (e.g., fatty acid β-oxidation), and heme b biosynthesis (Fig. 3C). Notably, reductive TCA cycle I and multiple heme b biosynthesis pathways were highly enriched, suggesting that the CRC group's microbiota may have enhanced overall capacity in redox metabolism, energy acquisition, and iron-heme utilization (Fig. 3C).

3.4 Multivariate Statistics and Differential Metabolite Characteristics of Metabolome Under Positive/Negative Ion Modes

Unsupervised PCA analysis unveiled that samples of CRC and HC groups exhibited a partial separation trend under both positive and negative ion modes, but there was obvious overlap within groups (Fig. 4A,B). In contrast, supervised OPLS-DA analysis achieved clear separation of the two groups under both ion modes. The negative ion mode had a higher model explanatory power (Q^2Y), indicating better differentiation of metabolic differences in this mode (Fig. 4C,D). Differential metabolite screening results identified 51 upregulated and 70 downregulated metabolites in the negative ion mode, and 46 upregulated and 82 downregulated metabolites in the positive ion mode (Fig. 4E,F). Volcano plots visually displayed the distribution of differential metabolites with orange dots representing metabolites upregulated in the CRC group, and blue dots representing downregulated ones (Fig. 4E,F).

3.5 Functional Enrichment Characteristics of Differential Metabolites

KEGG enrichment results showed that differential metabolites in the CRC group were mainly enriched in core pathways such as central carbon metabolism (cancer-related), amino acid metabolism, and lipid metabolism (Fig. 5A). Meanwhile, abnormalities in pathways including D-amino acid metabolism and GABAergic synapses indicated specific metabolic dysfunction in CRC patients (Fig. 5A). MetaCyc enrichment analysis further refined pathway characteristics: upregulated differential metabolites were enriched in amino acid metabolism and energy precursor generation-related pathways (Fig. 5B), while downregulated differential metabolites were enriched in the fatty acid and lipid biosynthesis pathway (Fig. 5C).

3.6 Association and Functional Validation of Microbiota-Metabolite Common Pathways

To elucidate microbiota–metabolite interactions in CRC, we performed an intersection analysis of microbiota functional pathways (predicted by 16S rRNA sequencing) and metabolite pathways (enriched by MetaCyc). Upregulated and downregulated pathways were analyzed separately to identify overlapping pathways within each (Fig. 6A,B). Only one significant common pathway was identified for both upregulation and downregulation: AST-PWY-arginine degradation II was commonly upregulated, and PWY-5392-reductive TCA cycle II (Fig. 6A,B) was commonly downregulated. These findings suggest that microbiota and metabolite perturbations in CRC are not independent but rather exhibit coordinated changes in specific core metabolic pathways. It is important to note that the 16S rRNA sequencing data and metabolomics data were derived from independent patient cohorts. Therefore, the association between *Lachnospiraceae* abundance and malate levels represents a co-pathway inference rather than a direct within-sample correlation.

We then identified key bacterial drivers of the common pathways using volcano plots. In the arginine degradation pathway, *Pseudomonas guguanensis* showed a significantly greater contribution in the CRC group compared with the HC group, establishing it as the primary driver (Fig. 6C). Conversely, the reductive TCA cycle pathway was primarily driven by beneficial genera enriched in the HC group such as *Dorea* and *Lachnospiraceae* (Fig. 6D). These results indicated that the "pathogen enrichment and beneficial bacteria depletion" in microbiota composition directly underlies the functional abnormalities of common pathways.

Finally, we validated the expression of metabolites enriched in the common pathways. Arginine levels were higher in the CRC group, while reductive TCA cycle-related metabolites (alpha-ketoglutarate, malate, succinate) were lower in the CRC group (Fig. 6E, $p < 0.01$). These results fully aligned with the pathway changes predicted by microbiota functions, further confirming the functional disruption of common pathways. In conclusion, structural changes in the intestinal microbiota and metabolite perturbations in CRC patients were closely and directly linked in core pathways such as arginine degradation and the reductive TCA cycle.

3.7 Lachnospiraceae Bacterium BAA-2278 Inhibited the Progression of CRC in Mice

Macroscopic observation of colon tissues first revealed a marked reduction in both the number and size of visible tumors in Lb-treated mice compared to the BHI controls (Fig. 7A). Quantitative analysis further confirmed a significant decrease in tumor number and tumor load (Fig.

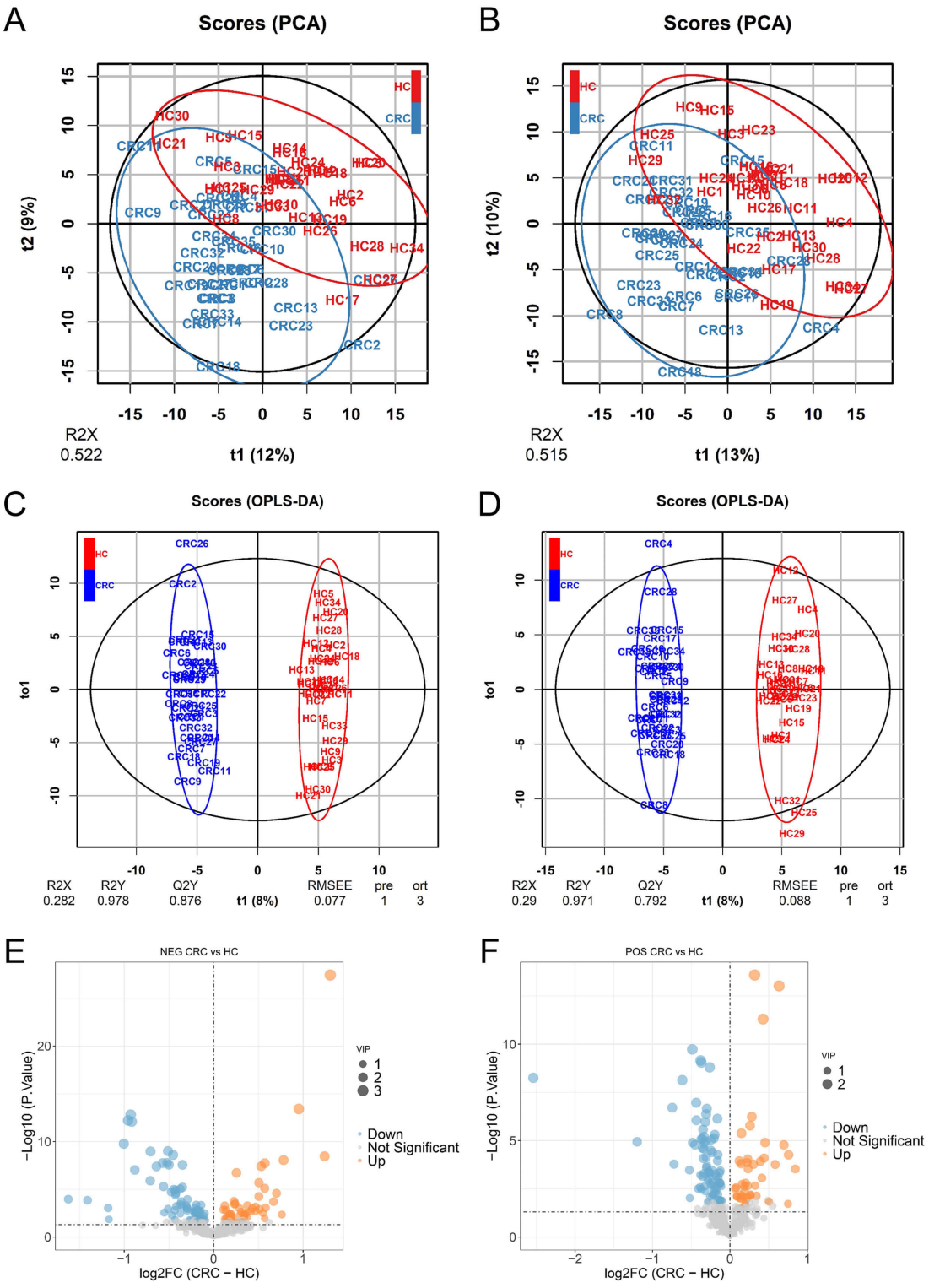

Fig. 4. Multivariate statistics and differential metabolites of serum metabolome under positive/negative ion modes. (A,B) Principal Component Analysis (PCA) score plots. (A) Negative ion mode. (B) Positive ion mode. Samples (colored by group: red = HC, blue = CRC) showed partial separation with intergroup overlap. (C,D) Orthogonal Partial Least Squares-Discriminant Analysis (OPLS-DA) score plots. (C) Negative ion mode. (D) Positive ion mode. Clear intergroup separation was achieved (higher Q^2Y in negative ion mode). (E,F) Volcano plots of differential metabolites. (E) Negative ion mode. (F) Positive ion mode. x-axis: $\log_2$ fold change (FC) (CRC vs. HC); y-axis: $-\log_{10}(p\text{-value})$. Orange dots: upregulated metabolites; blue dots: downregulated metabolites ($|\log_2 FC| > 0$, $p < 0.05$, Variable Importance in Projection (VIP) >1).

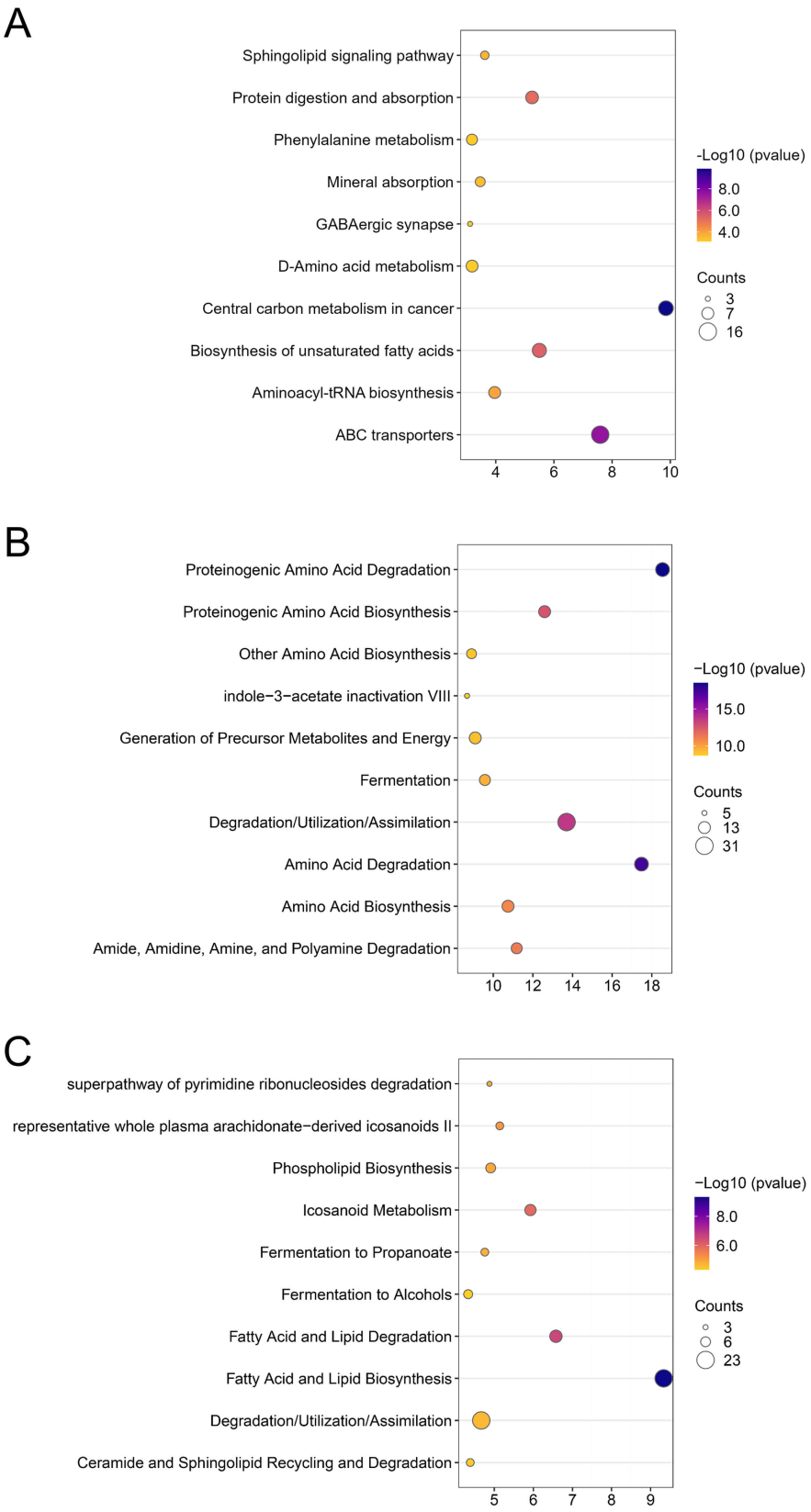

Fig. 5. Functional enrichment analysis of differential metabolites. (A) Kyoto Encyclopedia of Genes and Genomes (KEGG) pathway enrichment bubble plot. x-axis: number of differential metabolites in pathway; y-axis: pathway name; bubble size: metabolite count; color: $-\log_{10}(p\text{-value})$. (B) MetaCyc enrichment bubble plot (upregulated metabolites). x-axis: metabolite count; y-axis: pathway name; bubble size: metabolite count; color: $-\log_{10}(p\text{-value})$. (C) MetaCyc enrichment bubble plot (downregulated metabolites). x-axis: metabolite count; y-axis: pathway name; bubble size: metabolite count; color: $-\log_{10}(p\text{-value})$. ABC, ATP-binding cassette.

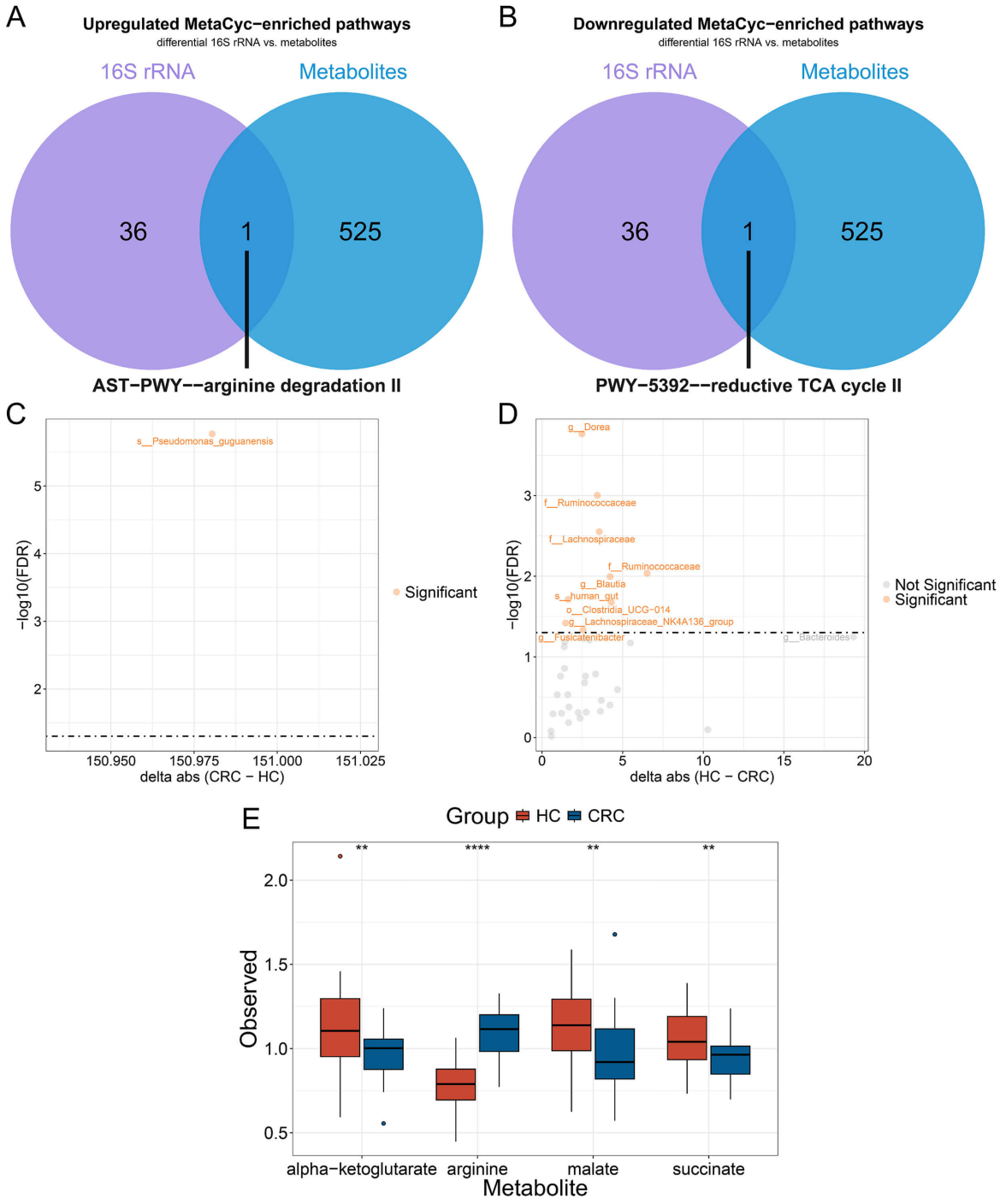

Fig. 6. Correlation and functional validation of microbiota-metabolite common pathways. (A,B) Venn diagrams of MetaCyc-enriched pathways. (A) Upregulated pathways (1 overlap: AST-PWY-arginine degradation II). (B) Downregulated pathways (1 overlap: PWY-5392--reductive TCA cycle II). Purple: microbiota pathways; blue: metabolite pathways. (C,D) Volcano plots of pathway-contributing bacteria. (C) Upregulated pathway (arginine degradation II): *Pseudomonas guguanensis* acted as a primary contributor. (D) Downregulated pathway (reductive TCA cycle II): Beneficial bacteria (e.g., *Dorea*, *Lachnospiraceae*) in HC were the main contributors. (E) Boxplots of common pathway metabolites. Metabolite levels shown are comparisons between HC and CRC groups within the Gao metabolomics cohort only. The association with microbiota is inferred through co-pathway analysis (functional intersection), not direct statistical correlation. CRC showed higher arginine levels and lower levels of alpha-ketoglutarate, malate, and succinate ($^{**}p < 0.01$, $^{****}p < 0.001$). AST, aspartate aminotransferase; PWY, pathway; TCA, tricarboxylic acid.

7B,C, $p < 0.05$). Histological examination via HE staining demonstrated reduced hyperplasia and cellular atypia in tumor tissues from Lb-treated animals (Fig. 7D). Ki-67 immunohistochemistry (positive signal: brown-yellow) confirmed substantial inhibition of tumor cell proliferation (Fig. 7F,H, $p < 0.01$). Concurrently, TUNEL staining (positive signal: brown-yellow) indicated that Lb treatment apparently enhanced tumor cell apoptosis (Fig. 7E,G, $p < 0.001$). Importantly, the concentration of D-malate in colon tissues was higher in the Lb-treated group than in BHI group (Fig. 7I, $p < 0.05$), which validated our previous bioinformatic findings that malate was downregulated in CRC.

3.8 Lachnospiraceae Bacterium BAA-2278 and Malate Suppressed CRC Cell Proliferation and Induced Apoptosis In Vitro

To investigate whether Lachnospiraceae directly produces malate, we measured the concentration of D-malate in the bacterial culture supernatant using a biochemical enzymatic colorimetric assay. D-malate concentration was significantly higher in Lachnospiraceae culture supernatants than in sterile BHI controls (Fig. 8A, $p < 0.001$). To determine the optimal concentration of D-malate for subsequent experiments, CCK-8 assay was performed using a concentration gradient. D-malate inhibited HCT116 cell viability in a dose-dependent manner, with an IC_{50} of approximately 15 mM (Fig. 8B); therefore, 15 mM was selected as the working concentration.

To verify whether the anti-CRC effects of malate are mediated through the Wnt/β-catenin pathway, β-catenin overexpression rescue experiments were performed. Western blot confirmed successful transfection of pcDNA3.1-β-catenin, with β-catenin expression significantly elevated compared to the empty vector control (NC) (Fig. 8C, $p < 0.05$). In in vitro assays, treatment with Lb-CM or malate significantly reduced the relative viability of CRC cells (HCT116) compared with the BHI group, β-catenin overexpression partially restored cell viability reduced by malate treatment (Fig. 8D, $p < 0.001$). EdU staining (red fluorescence, marking actively proliferating cells) further confirmed marked inhibition of cell proliferation activity by Lb-CM or malate, β-catenin overexpression reversed the proliferation inhibition induced by malate (Fig. 8E,G, $p < 0.001$), while flow cytometry results demonstrated that both treatments robustly induced tumor cell apoptosis, β-catenin overexpression attenuated malate-induced apoptosis (Fig. 8F,H, $p < 0.001$). Collectively, these findings support that *Lachnospiraceae* bacterium BAA-2278 and its metabolite malate exerted anti-tumor effects *in vitro* by suppressing cell proliferation and promoting apoptosis.

3.9 Lachnospiraceae Bacterium BAA-2278 and Malate Repressed CRC Cell Colony Formation and Wingless/Integrated (Wnt)/β-Catenin Signaling In Vitro

In vitro colony formation assays revealed that treatment with Lb-CM or malate dramatically reduced the number of cell colonies compared with the BHI group, β-catenin overexpression significantly restored colony formation capacity suppressed by malate treatment (Fig. 9A,E, $p < 0.01$). Western blot analysis further demonstrated that both treatments significantly diminished the protein expression levels of key Wnt/β-catenin signaling pathway-related factors, including β-catenin, c-Myc, and MMP7, β-catenin overexpression reversed the downregulation of β-catenin, c-Myc, and MMP7 induced by malate (Fig. 9B–D,F, $p < 0.05$). These results indicated that *Lachnospiraceae* and its metabolite malate exerted anti-tumor effects *in vitro* by dampening cell colony formation and the oncogenic Wnt/β-catenin signaling pathway.

4. Discussion

Functional microbiota and their metabolites deeply participate in CRC pathogenesis by remodeling the intestinal microenvironment and regulating host signaling pathways [24]. *Lachnospiraceae*, an abundant commensal beneficial bacterial family in the gut, has been linked to reduced CRC risk [25]. This study proposes a novel potential anti-CRC regulatory axis mechanism: bioinformatics analysis of patient samples revealed that *Lachnospiraceae* depletion was pertinent to malate downregulation in CRC. *In vivo* and *in vitro* experiments demonstrated *Lachnospiraceae* and malate restored gut microbiota homeostasis, while inhibiting CRC cell proliferation and Wnt/β-catenin pathway.

Bioinformatics analysis served as a pivotal tool for deciphering microbiota-metabolite associations. In this study, by integrating 16S rRNA gene functional prediction and metabolomic data, we identified an association between Lachnospiraceae abundance and malate levels in CRC patient samples, though this association was inferred from independent cohorts rather than derived from direct correlations within paired samples. Notably, the intestinal malate levels were remarkably reduced in CRC patients, concurrent with microbial dysbiosis characterized by decreased *Lachnospiraceae* abundance. This finding aligned with previous conclusions that CRC patients exhibited abnormal metabolic profiles and reduced abundance of beneficial bacteria [26,27]. Furthermore, alterations in levels of malate, as a critical intermediate of the tricarboxylic acid cycle, not only reflect the characteristics of tumor metabolic reprogramming [28,29], but also implicate *Lachnospiraceae* abundance as a core driver of the abnormal expression of this metabolite, thus defining the research targets for subsequent *in vitro* and *in vivo* experiments.

In this study, treatment with *Lachnospiraceae* bacterium BAA-2278 effectively restored the homeostasis of intestinal microbiota in CRC AOM/DSS-induced mice, reduced the number of tumors and decreased tumor load. Ki67, a specific marker for cell proliferation, is also significantly downregulated after *Lachnospiraceae* treatment [30]. In addition, elevated D-malate levels in colon tissues following *Lachnospiraceae* treatment verified the bioinfor-

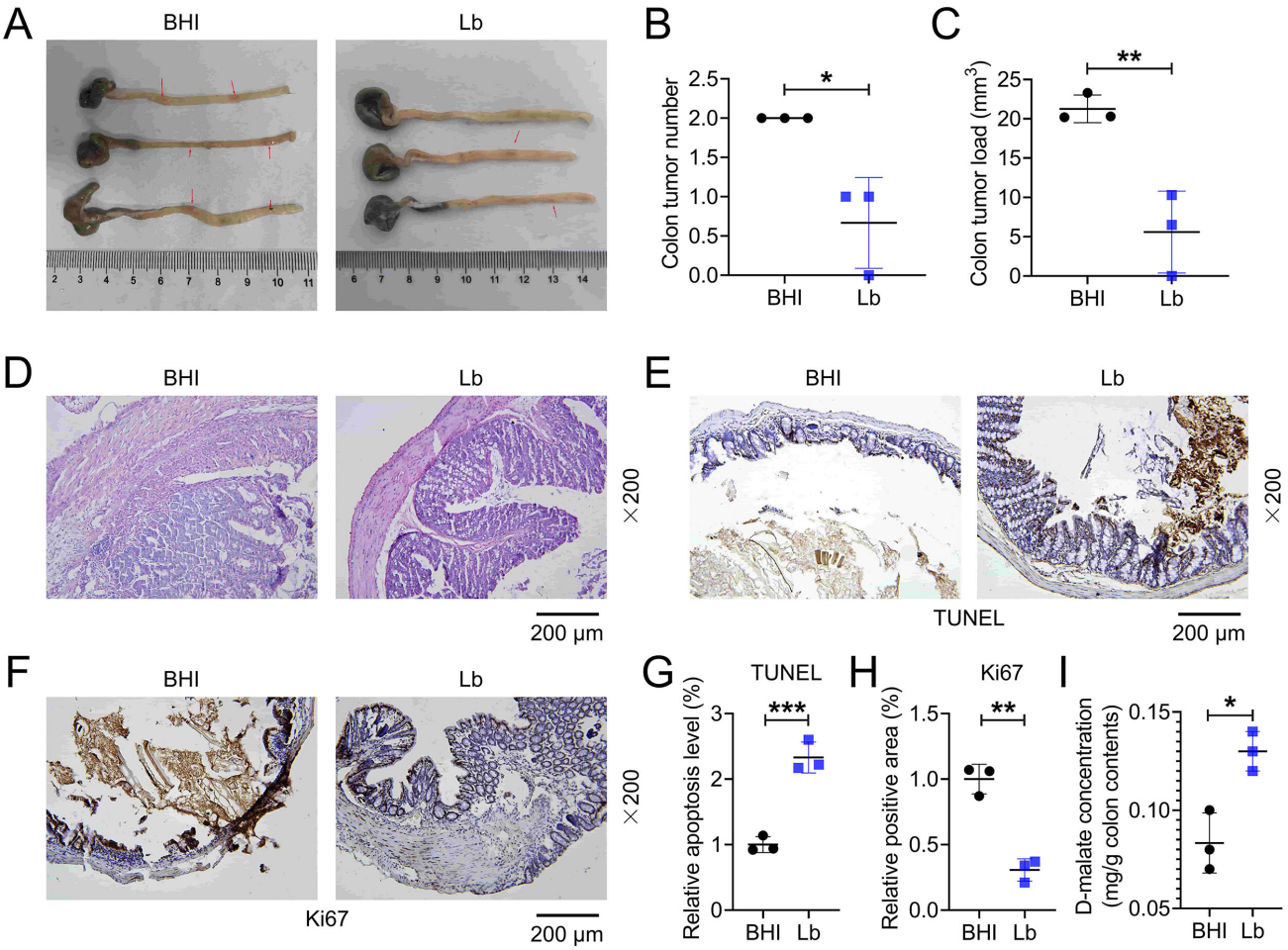

Fig. 7. *Lachnospiraceae* bacterium BAA-2278 (Lb) treatment suppressed colorectal tumorigenesis *in vivo* and induced D-malate accumulation. (A) Macroscopic observation of colon contents from brain heart infusion (BHI) controls and Lb-treated mice. (B) Quantitative analysis of colon tumor number. (C) Quantitative analysis of total colon tumor load. (D) Hematoxylin and eosin (HE) staining of colon tumor sections (magnification: ×200, scale bar: 200 μm). (E) Terminal Deoxynucleotidyl Transferase mediated dUTP Nick-End Labeling (TUNEL) staining for apoptotic cells (positive signal: brown-yellow) in colon tumor sections (magnification: ×200, scale bar: 200 μm). (F) MKi-67 (Ki67) immunohistochemical staining for proliferative cells (positive signal: brown-yellow) in colon tumor sections (magnification: ×200, scale bar: 200 μm). (G) Quantitative analysis of relative apoptosis level from TUNEL staining. (H) Quantitative analysis of Ki-67-positive area. (I) Concentration of D-malate in colon contents. Each group contained 8 mice. Data are presented as mean ± standard deviation (SD) (n = 3 independent experiments). $^{*}p < 0.05$, $^{**}p < 0.01$, $^{***}p < 0.001$ vs. the BHI group.

matic hypothesis that "*Lachnospiraceae* secretes malate". Existing studies have shown that microbe-derived D-malate can affect cell proliferation by regulating the acetylation of cyclins [23], which also provides a logical basis for the direct use of malate in subsequent *in vitro* experiments.

In vitro assays elucidated the mechanism of the *Lachnospiraceae*-malate axis at the molecular level. Both D-malate and *Lachnospiraceae* bacterial supernatant inhibited CRC cell proliferation, induced apoptosis and suppressed colony formation, consistent with previous findings that malate preserves the function of cytotoxic T cells in the tumor microenvironment [31]. These results suggested that its anti-tumor effects were related to both cell-autonomous regulation and immunomodulation. More importantly, both treatments inhibited the protein expression of β-catenin, c-Myc and MMP7 in the Wnt/β-catenin pathway, which is known to ameliorate CRC progression when inhibited [32,33]. β-catenin acts as a core transcription factor of this pathway, c-Myc drives cell cycle progression, and MMP7 enhances tumor invasion by degrading the extracellular matrix [34]. These findings elucidate a potential mechanism by which the *Lachnospiraceae*-malate axis may contribute to blocking CRC progression through inhibiting Wnt/β-catenin pathway activity.

Regarding the functional differences between reductive TCA cycle I and II, this apparent inconsistency does not represent a true biological discrepancy but rather arises from different analytical dimensions. Based on 16S rRNA sequencing and PICRUSt2 functional prediction, Fig. 3C shows that reductive TCA cycle I (P23-PWY) is ranked

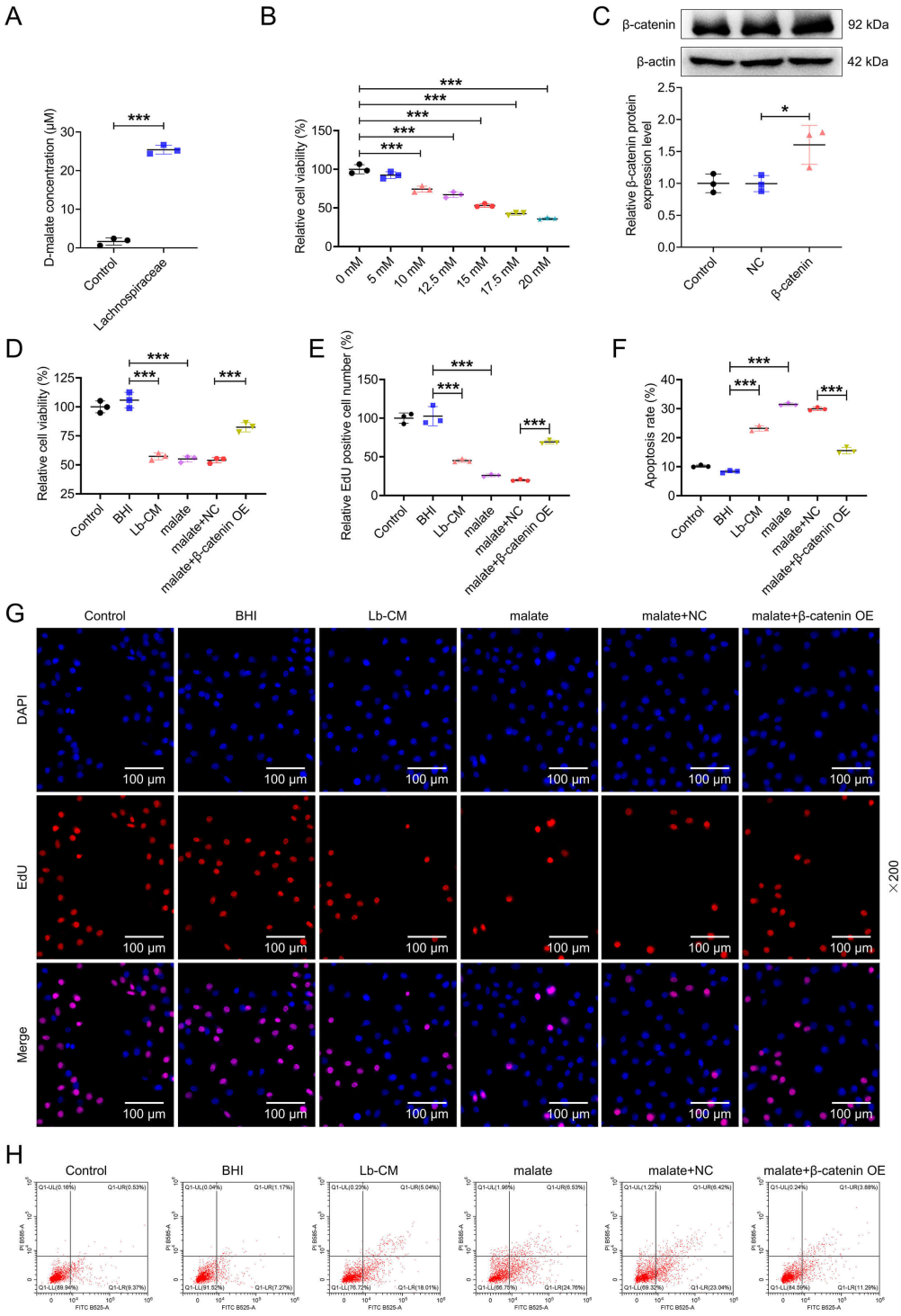

Fig. 8. *Lachnospiraceae* bacterium BAA-2278-derived conditioned medium (Lb-CM) and malate suppressed CRC cell proliferation and induced apoptosis *in vitro*. (A) The concentration of D-malate in Lachnospiraceae bacterial culture supernatant was measured using a biochemical enzymatic colorimetric assay. (B) The effect of D-malate at various concentrations on HCT116 cell viability was assessed by CCK-8 assay. (C) Western blot was performed to verify the transfection efficiency of pcDNA3.1-β-catenin. (D) Relative cell viability of each group. (E) Quantification of 5-Ethynyl-2′-deoxyuridine (EdU)-positive cells. (F) Quantitative analysis of apoptosis rate. (G) EdU staining for cell proliferation (4′,6-Diamidino-2′-phenylindole (DAPI) staining labels all cell nuclei in blue; EdU staining labels actively proliferating cells in red; magnification: ×200, scale bar: 100 μm). (H) Dot plots of apoptosis detected by flow cytometry. Data are presented as mean ± SD (n = 3 independent experiments). $^{*}p < 0.05$, $^{***}p < 0.001$ vs. the BHI group. NC, negative control; OE, overexpression.

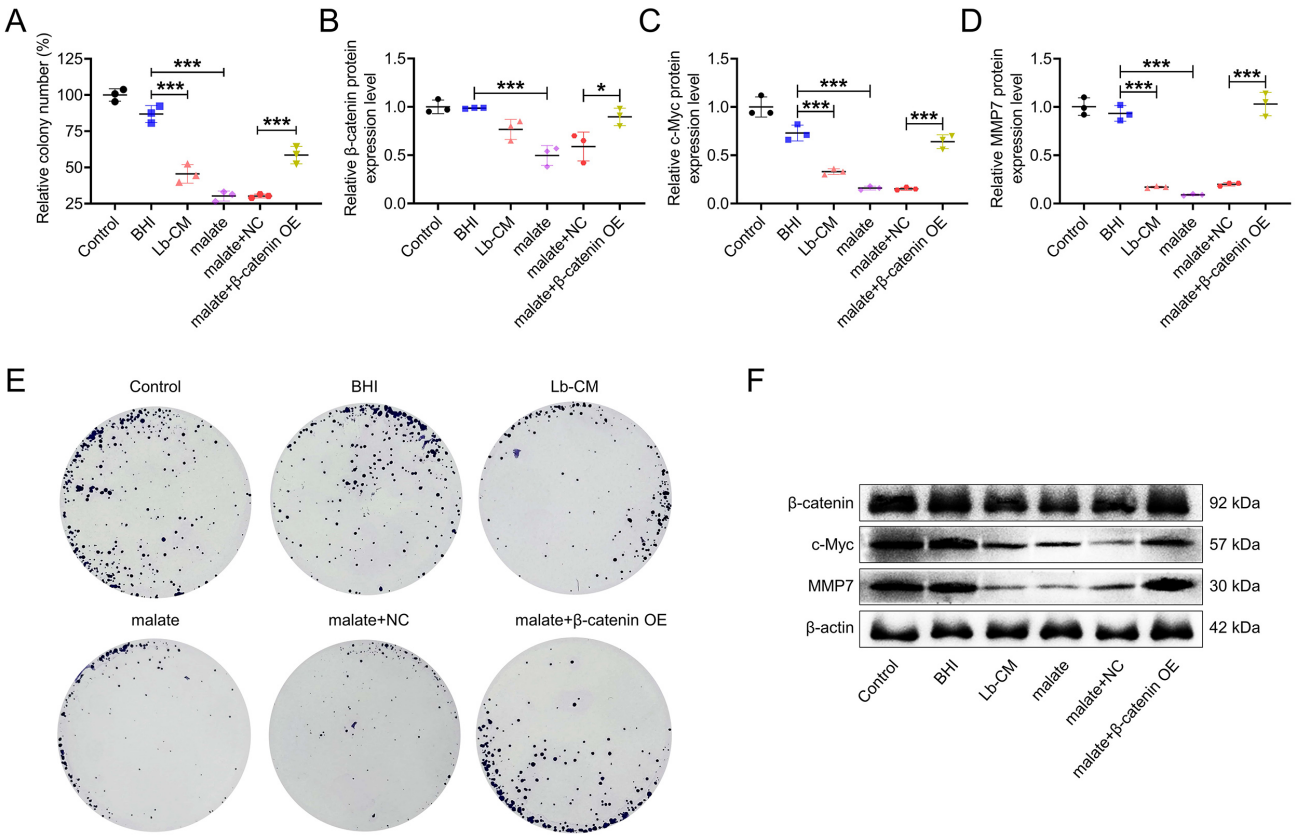

Fig. 9. Lb-CM and malate repressed CRC cell colony formation and Wingless/Integrated (Wnt)/β-catenin signaling *in vitro*. (A,E) Cell proliferation was detected by colony formation. (B–D,F) Western blot analysis of β-catenin, Myelocytomatosis oncogene (c-Myc) and matrix metallopeptidase 7 (MMP7), with β-actin as a loading control. Data are presented as mean ± SD (n = 3 independent experiments). $^{*}p < 0.05$, $^{***}p < 0.001$ vs. the BHI group.

among the top 20 upregulated microbial pathways in the CRC group, suggesting an elevated gene abundance of this pathway that is mainly associated with enhanced metabolic activity of pathogenic bacteria such as Pseudomonas. Further cross-dataset analysis in Fig. 6B indicates that reductive TCA cycle II (PWY-5392) is the only commonly downregulated pathway after integrating differential pathways from 16S sequencing and metabolomic data. These findings reflect suppressed activity of reductive TCA cycle II in CRC, and its downstream metabolites including malate, α-ketoglutarate and succinate are markedly reduced in patient serum, which is consistent with the decreased abundance of beneficial Lachnospiraceae. The combination of single-dataset pathway screening and cross-dataset functional validation effectively improves the robustness of our bioinformatic conclusions.

5. Limitations

Several limitations of this study should be acknowledged. First, our bioinformatic analysis relied on 16S rRNA sequencing data and metabolomics data from two independent patient cohorts, which precluded direct correlation analysis between *Lachnospiraceae* abundance and malate levels within the same samples. Although co-pathway analysis identified consistent functional alterations across datasets, and subsequent *in vivo* and *in vitro* experiments provided causal and mechanistic validation, paired-sample validation remains essential to definitively establish the *Lachnospiraceae*-malate axis in future work. Second, while our *in vivo* experiments demonstrated that oral administration of live *Lachnospiraceae* significantly elevated colonic D-malate concentration and suppressed tumor progression, we did not directly perform genetic knockout of putative malate synthesis pathways, or conduct isotopic tracing experiments to confirm the bacterial origin of malate. Third, the *in vivo* experimental design carries inherent constraints: we did not characterize baseline microbiota composition prior to *Lachnospiraceae* intervention, include heat-killed bacterial controls or sterile filtrate controls, or employ germ-free or antibiotic-treated mice to isolate microbiota-dependent effects. Additionally, the use of a single bacterial strain (BAA-2278) limits generalization to the entire *Lachnospiraceae* family, and the sample size of eight mice per group, while standard for gut microbiota intervention studies, may be underpowered for detecting moderate effect sizes given the expected inter-individual

variation in microbiota. Fourth, regarding the translational potential of malate, this study represents a proof-of-concept for the *Lachnospiraceae*-malate-Wnt/β-catenin regulatory axis rather than a preclinical drug development program. We did not assess oral bioavailability, pharmacokinetic profiles, or chronic toxicity of malate, nor did we compare efficacy against standard-of-care CRC therapies such as 5-FU or oxaliplatin. The poor oral bioavailability of malate may necessitate colon-targeted delivery systems to achieve therapeutic concentrations at the luminal surface, and comprehensive toxicity assessment in chronic administration models should be pursued before clinical translation can be considered. Finally, our bioinformatic analysis did not fully clarify the specific molecular mechanisms by which *Lachnospiraceae* regulates malate production, nor did it explore potential synergistic or antagonistic effects of other gut microbiota on this regulatory axis. These limitations define the boundary between mechanistic discovery and translational development, and addressing them will be the focus of our future investigations.

6. Conclusions

In summary, integrating bioinformatics with *in vivo* and *in vitro* experimental validation, this study provides evidence supporting how the "*Lachnospiraceae* bacterium BAA-2278-malate-intestinal microbiota" regulatory axis may exert anti-CRC effects in experimental settings and confirmed that *Lachnospiraceae* bacterium BAA-2278 exerts anti-tumor effects by secreting malate to restore gut microbiota homeostasis and inhibit the activity of the Wnt/β-catenin pathway. Future studies should prioritize the identification of *Lachnospiraceae* genes involved in malate synthesis, investigate the clinical translational value of malate, and verify the generalizability of this regulatory axis across multiple cell lines and clinical samples, so as to provide a more solid theoretical basis for microecology-targeted intervention in CRC.

Availability of Data and Materials

The datasets generated and/or analysed during the current study are not publicly available due to privacy concerns, but are available from the corresponding author on reasonable request.

Author Contributions

ZJF, YYH, and MJZ designed the research study; HMM and CJG performed the research, and JEC analyzed the data; ZJF and YYH participated in writing the initial draft. All authors contributed to editorial changes in the manuscript. All authors read and approved the final manuscript. All authors have participated sufficiently in the work and agreed to be accountable for all aspects of the work.

Ethics Approval and Consent to Participate

The animal experiments conducted in this study strictly adhered to the Guidelines for Ethical Review of Laboratory Animal Welfare and were approved by the Laboratory Animal Ethics Review Committee of Zhejiang Provincial Laboratory Animal Center (ZJCLA-IACUC-20011391). The study was carried out in accordance with the ARRIVE guidelines.

Acknowledgment

Not applicable.

Funding

This work was supported by the National Natural Science Foundation of China (grant number: 82303594), Zhejiang Medical and Health Science and Technology Plan (grant number: 2024XY091) and Zhejiang Provincial County Level Advantageous Disciplines of Traditional Chinese Medicine Construction Plan (grant number: 2023-XK-D040).

Conflicts of Interest

The authors declare no conflicts of interest.

Supplementary Material

Supplementary material associated with this article can be found, in the online version, at https://doi.org/10.31083/FBL52075.

References

[1] Zhao W, Dai S, Yue L, Xu F, Gu J, Dai X, et al. Emerging mechanisms progress of colorectal cancer liver metastasis. Frontiers in Endocrinology. 2022; 13: 1081585. https://doi.org/10.3389/fendo.2022.1081585

[2] Ning Z, Yang X, Gao K, Cao Y, Shen L. Research progress on the mechanisms of traditional Chinese medicine extracts-induced oxidative stress in the treatment of colorectal cancer. Guidelines and Standards of Chinese Medicine. 2025; 3: 106–112. https://doi.org/10.1097/gscm.0000000000000057

[3] Qu R, Zhang Y, Ma Y, Zhou X, Sun L, Jiang C, et al. Role of the Gut Microbiota and Its Metabolites in Tumorigenesis or Development of Colorectal Cancer. Advanced Science (Weinheim, Baden-Wurttemberg, Germany). 2023; 10: e2205563. https://doi.org/10.1002/advs.202205563

[4] Wang Z, Dan W, Zhang N, Fang J, Yang Y. Colorectal cancer and gut microbiota studies in China. Gut Microbes. 2023; 15: 2236364. https://doi.org/10.1080/19490976.2023.2236364

[5] Cheng Y, Ling Z, Li L. The Intestinal Microbiota and Colorectal Cancer. Frontiers in Immunology. 2020; 11: 615056. https://doi.org/10.3389/fimmu.2020.615056

[6] Ionescu VA, Diaconu CC, Gheorghe G, Mihai MM, Diaconu CC, Bostan M, et al. Gut Microbiota and Colorectal Cancer: A Balance Between Risk and Protection. International Journal of Molecular Sciences. 2025; 26: 3733. https://doi.org/10.3390/ijms26083733

[7] Huang F, Li S, Chen W, Han Y, Yao Y, Yang L, et al. Postoperative Probiotics Administration Attenuates Gastrointestinal Complications and Gut Microbiota Dysbiosis Caused by Chemother-

apy in Colorectal Cancer Patients. Nutrients. 2023; 15: 356. https://doi.org/10.3390/nu15020356

[8] Hexun Z, Miyake T, Maekawa T, Mori H, Yasukawa D, Ohno M, et al. High abundance of Lachnospiraceae in the human gut microbiome is related to high immunoscores in advanced colorectal cancer. Cancer Immunology, Immunotherapy: CII. 2023; 72: 315–326. https://doi.org/10.1007/s00262-022-03256-8

[9] Zhang X, Yu D, Wu D, Gao X, Shao F, Zhao M, et al. Tissue-resident Lachnospiraceae family bacteria protect against colorectal carcinogenesis by promoting tumor immune surveillance. Cell Host & Microbe. 2023; 31: 418–432.e8. https://doi.org/10.1016/j.chom.2023.01.013

[10] Zong G, Deng R, Pan Y, Liu M, Zhu H, Tao R, et al. Ginseng polysaccharides ameliorate colorectal tumorigenesis through Lachnospiraceae-mediated immune modulation. International Journal of Biological Macromolecules. 2025; 307: 142015. https://doi.org/10.1016/j.ijbiomac.2025.142015

[11] Zhao K, Zhang F, Qin Q, Zhang D, Yang F, Huang Y, et al. Malate targets pyruvate kinase M2 to promote colorectal cancer cell cycle arrest and tumor suppression. Molecular Biomedicine. 2025; 6: 79. https://doi.org/10.1186/s43556-025-00326-y

[12] Chen M, Zhao Y, Li S, Chang Z, Liu H, Zhang D, et al. Maternal Malic Acid May Ameliorate Oxidative Stress and Inflammation in Sows through Modulating Gut Microbiota and Host Metabolic Profiles during Late Pregnancy. Antioxidants (Basel, Switzerland). 2024; 13: 253. https://doi.org/10.3390/antiox13020253

[13] Kumar A, Delgoffe GM. Redox and detox: Malate shuttle metabolism keeps exhausted T cells fit. Cell Metabolism. 2023; 35: 2101–2103. https://doi.org/10.1016/j.cmet.2023.11.005

[14] Ternes D, Tsenkova M, Pozdeev VI, Meyers M, Koncina E, Atatri S, et al. The gut microbial metabolite formate exacerbates colorectal cancer progression. Nature metabolism. 2022; 4: 458–475. https://doi.org/10.1038/s42255-022-00558-0

[15] Gao R, Wu C, Zhu Y, Kong C, Zhu Y, Gao Y, et al. Integrated Analysis of Colorectal Cancer Reveals Cross-Cohort Gut Microbial Signatures and Associated Serum Metabolites. Gastroenterology. 2022; 163: 1024–1037.e9. https://doi.org/10.1053/j.gastro.2022.06.069

[16] Nayfach S, Roux S, Seshadri R, Udwary D, Varghese N, Schulz F, et al. A genomic catalog of Earth's microbiomes. Nature Biotechnology. 2021; 39: 499–509. https://doi.org/10.1038/s41587-020-0718-6

[17] Douglas GM, Maffei VJ, Zaneveld JR, Yurgel SN, Brown JR, Taylor CM, et al. PICRUSt2 for prediction of metagenome functions. Nature Biotechnology. 2020; 38: 685–688. https://doi.org/10.1038/s41587-020-0548-6

[18] Louca S, Parfrey LW, Doebeli M. Decoupling function and taxonomy in the global ocean microbiome. Science (New York, N.Y.). 2016; 353: 1272–1277. https://doi.org/10.1126/science.aaf4507

[19] Leung HKM, Lo EKK, El-Nezami H. Theabrownin Alleviates Colorectal Tumorigenesis in Murine AOM/DSS Model via PI3K/Akt/mTOR Pathway Suppression and Gut Microbiota Modulation. Antioxidants (Basel, Switzerland). 2022; 11: 1716. https://doi.org/10.3390/antiox11091716

[20] Su ACY, Ding X, Lau HCH, Kang X, Li Q, Wang X, et al. *Lactococcus lactis HkyuLL 10* suppresses colorectal tumourigenesis and restores gut microbiota through its generated alpha-mannosidase. Gut. 2024; 73: 1478–1488. https://doi.org/10.1136/gutjnl-2023-330835

[21] Zhang H, Hu Q, Zhang Y, Yang L, Tian S, Zhang X, et al. *Lachnospiraceae bacterium* alleviates alcohol-associated liver disease by enhancing N-acetyl-glutamic acid levels and inhibiting ferroptosis through the KEAP1-NRF2 pathway. Gut Microbes. 2025; 17: 2517821. https://doi.org/10.1080/19490976.2025.2517821

[22] Hsiao YP, Lai WW, Wu SB, Tsai CH, Tang SC, Chung JG, et al. Triggering apoptotic death of human epidermal keratinocytes by malic Acid: involvement of endoplasmic reticulum stress- and mitochondria-dependent signaling pathways. Toxins. 2015; 7: 81–96. https://doi.org/10.3390/toxins7010081

[23] Li P, Feng J, Jiang H, Feng X, Yang J, Yuan Y, et al. Microbiota derived D-malate inhibits skeletal muscle growth and angiogenesis during aging via acetylation of Cyclin A. EMBO Reports. 2024; 25: 524–543. https://doi.org/10.1038/s44319-023-00028-y

[24] Thulasinathan B, Suvilesh KN, Maram S, Grossmann E, Ghouri Y, Teixeiro EP, et al. The impact of gut microbial short-chain fatty acids on colorectal cancer development and prevention. Gut Microbes. 2025; 17: 2483780. https://doi.org/10.1080/19490976.2025.2483780

[25] De Filippo C, Chioccioli S, Meriggi N, Troise AD, Vitali F, Mejia Monroy M, et al. Gut microbiota drives colon cancer risk associated with diet: a comparative analysis of meat-based and pesco-vegetarian diets. Microbiome. 2024; 12: 180. https://doi.org/10.1186/s40168-024-01900-2

[26] Chen J, Li Y, Tang S, Jin W, Yan R. Gut microbial β-glucuronidases and their role in the microbiome-metabolite axis in colorectal cancer. Nature Communications. 2025; 16: 10660. https://doi.org/10.1038/s41467-025-65679-y

[27] Pramana AAC, Xu GB, Liang S, Garcia Vazquez EO, Allen JM, Loman BR, et al. Gut microbiota dysbiosis in a novel mouse model of colitis potentially increases the risk of colorectal cancer. American Journal of Physiology. Gastrointestinal and Liver Physiology. 2025; 328: G831–G847. https://doi.org/10.1152/ajpgi.00040.2025

[28] Guo D, He H, Meng Y, Luo S, Lu Z. Determiners of cell fates: the tricarboxylic acid cycle versus the citrate-malate shuttle. Protein & Cell. 2023; 14: 162–164. https://doi.org/10.1093/procel/pwac026

[29] Astorga J, Gasaly N, Dubois-Camacho K, De la Fuente M, Landskron G, Faber KN, et al. The role of cholesterol and mitochondrial bioenergetics in activation of the inflammasome in IBD. Frontiers in Immunology. 2022; 13: 1028953. https://doi.org/10.3389/fimmu.2022.1028953

[30] Kitsel Y, Cooke T, Sotirchos V, Sofocleous CT. Colorectal Cancer Liver Metastases: Genomics and Biomarkers with Focus on Local Therapies. Cancers. 2023; 15: 1679. https://doi.org/10.3390/cancers15061679

[31] Weisshaar N, Ma S, Ming Y, Madi A, Mieg A, Hering M, et al. The malate shuttle detoxifies ammonia in exhausted T cells by producing 2-ketoglutarate. Nature Immunology. 2023; 24: 1921–1932. https://doi.org/10.1038/s41590-023-01636-5

[32] Zhao H, Ming T, Tang S, Ren S, Yang H, Liu M, et al. Wnt signaling in colorectal cancer: pathogenic role and therapeutic target. Molecular Cancer. 2022; 21: 144. https://doi.org/10.1186/s12943-022-01616-7

[33] Khan S, Kwak YT, Peng L, Hu S, Cantarel BL, Lewis CM, et al. NLRP12 downregulates the Wnt/β-catenin pathway via interaction with STK38 to suppress colorectal cancer. The Journal of Clinical Investigation. 2023; 133: e166295. https://doi.org/10.1172/JCI166295

[34] Shi S, Li C, Zhang Y, Deng C, Liu W, Du J, et al. Dihydrocapsaicin Inhibits Cell Proliferation and Metastasis in Melanoma *via* Down-regulating β-Catenin Pathway. Frontiers in Oncology. 2021; 11: 648052. https://doi.org/10.3389/fonc.2021.648052